

# Quantum Efficiency Enhancement of Lead-Halide Perovskite Nanocrystal LEDs by Organic Lithium Salt Treatment

Tassilo Naujoks, Roshini Jayabalan, Christopher Kirsch, Fengshuo Zu, Mukunda Mandal, Jan Wahl, Martin Waibel, Andreas Opitz, Norbert Koch, Denis Andrienko, Marcus Scheele, and Wolfgang Brütting\*



Cite This: *ACS Appl. Mater. Interfaces* 2022, 14, 28985–28996



Read Online

ACCESS |



Metrics & More



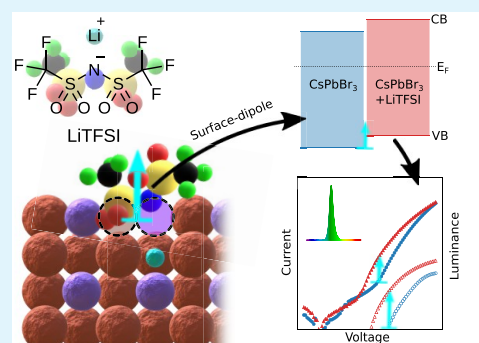
Article Recommendations



Supporting Information

**ABSTRACT:** Surface-defect passivation is key to achieving a high photoluminescence quantum yield in lead halide perovskite nanocrystals. However, in perovskite light-emitting diodes, these surface ligands also have to enable balanced charge injection into the nanocrystals to yield high efficiency and operational lifetime. In this respect, alkaline halides have been reported to passivate surface trap states and increase the overall stability of perovskite light emitters. On the one side, the incorporation of alkaline ions into the lead halide perovskite crystal structure is considered to counterbalance cation vacancies, whereas on the other side, the excess halides are believed to stabilize the colloids. Here, we report an organic lithium salt, viz. LiTFSI, as a halide-free surface passivation on perovskite nanocrystals. We show that treatment with LiTFSI has multiple beneficial effects on lead halide perovskite nanocrystals and LEDs derived from them. We obtain a higher photoluminescence quantum yield and a longer exciton lifetime and a radiation pattern that is more favorable for light outcoupling. The ligand-induced dipoles on the nanocrystal surface shift their energy levels toward a lower hole-injection barrier. Overall, these effects add up to a 4- to 7-fold boost of the external quantum efficiency in proof-of-concept LED structures, depending on the color of the used lead halide perovskite nanocrystal emitters.

**KEYWORDS:** perovskite nanocrystals, CsPbBr<sub>3</sub> nanocrystals, LiTFSI doping, perovskite LEDs, surface passivation



## 1. INTRODUCTION

Electroluminescent perovskite light-emitting devices (PeLED) were first reported in the 1990s and achieved external quantum efficiencies similar to state-of-the-art fluorescent organic LEDs at that time;<sup>1</sup> however, because of severe temperature-induced efficiency drop they have been operated at low temperature only, typically in liquid nitrogen.<sup>2</sup> Triggered by their success in photovoltaics, perovskites with the general formula ABX<sub>3</sub> (where A is a monovalent organic or inorganic cation, B a bivalent cation – typically Pb<sup>2+</sup> – and X a halide anion) have been “rediscovered” as light emitters less than a decade ago<sup>3</sup> and have developed into a rapidly progressing LED technology ever since.<sup>4–7</sup> Narrow emission bands, which are easily tunable by perovskite composition and size in the case of nanostructured materials, paired with high photo- and electroluminescence efficiency over the entire visible and near-infrared spectral range make them attractive candidates for next-generation displays and lighting. However, despite external quantum efficiencies of PeLEDs being close to organic LEDs, their practical use is still severely limited by insufficient operational lifetimes being on the order of a few 10–100 h at best.<sup>8,9</sup>

In the focus of this work are electroluminescent lead halide perovskite (LHP) nanocrystals (NC), which are, beside 3D

bulk and 2D layered perovskites, an emerging class of active light emitters for PeLEDs. They share attractive features like solution processability, ease of bandgap tuning and defect tolerance, however, with potentially higher radiative decay rates and, thus, higher photoluminescence quantum yield in the case of LHP NCs even in the absence of a core–shell structure. Nevertheless, NCs have particularly large surface-area-to-volume ratio, which makes them very sensitive toward surface defects and, thus, strategies to develop defect passivation are particularly important.<sup>10</sup> Consequently, surface chemistry plays a pivotal role in the optoelectronic properties of LHP NCs.

LHP NCs are typically synthesized as colloidal suspensions stabilized by organic ligands, such as oleic acid and oleylamine (see Figure 1).<sup>11</sup> Despite their high photoluminescence, these pristine “solutions” cannot be used directly for film fabrication

Received: March 4, 2022

Accepted: May 30, 2022

Published: June 13, 2022



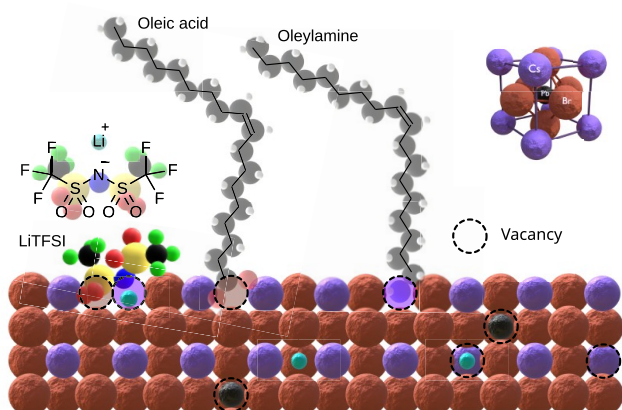


**Figure 1.** Schematic CsPbBr<sub>3</sub> NC surface with possible interaction mechanisms by oleic acid, oleylamine, and the organic lithium salt, LiTFSI. Li<sup>+</sup> may fill a vacancy or may be intercalated. On the upper right, a full PbBr<sub>6</sub> octahedron with adjacent Cs ions is depicted to illustrate the ABX<sub>3</sub> crystal structure.

and implementation in PeLEDs because of the electrically insulating nature of the ligands. Moreover, nonbinding excess ligands, required to stabilize the suspensions, even deteriorate charge injection into the NCs further.<sup>12–14</sup> “Washing” the nanocrystals before film deposition removes these ligands partially; however, it is at the expense of creating a large density of surface defects with the concomitant formation of nonradiative exciton decay channels mainly caused by A- and X-site vacancies, as well as inducing stability issues. To overcome these problems, researchers have developed a variety of different surface passivation strategies and employed them in LHP NCs, including halide salts, strongly binding organic ligands, and zwitterionic species.<sup>15–19</sup> In particular, the use of lithium halides has been shown to increase the photoluminescence yield as well as their stability.<sup>20</sup> Therein, its passivation is mostly attributed to the excess halides that fill the corresponding vacancies at the NC surface and, thus, reduce nonradiative defects and, at the same time, suppress ion migration via these vacancies. Nevertheless, the role of the Li<sup>+</sup> cation itself has largely remained elusive.<sup>21</sup> Thus, it is worth studying the effect of halide-free lithium salts, like lithium bis(trifluoromethanesulfonyl)imide (LiTFSI, see Figure 1), which has already been investigated as a beneficial additive in perovskite solar cells.<sup>22–24</sup> In this work, we show that by adding LiTFSI to various LHP NC solutions, with emission colors ranging from deep red to green to sky blue, their optoelectronic properties are tuned toward a higher photoluminescence quantum yield, better hole injection and transport, and a lower electroluminescence turn-on voltage. Overall, this results in a 4- to 7-fold increase of the external quantum efficiency of PeLEDs.

## 2. RESULTS AND DISCUSSION

**2.1. Surface Ligand Exchange.** LHP NCs with different stoichiometry and emission color, ranging from sky blue (CsPbBr<sub>2</sub>Cl) to green (CsPbBr<sub>3</sub>) to red (MAPbBr<sub>3</sub>, where MA stands for methylammonium), have been obtained commercially or synthesized as described in the Methods section. The native NC solutions with oleylamine and oleic acid surface ligands (10 mg/mL solid NC contents in toluene) have subsequently been mixed with equal volumes of LiTFSI solutions in chlorobenzene; see Methods for details. This has

resulted in different weight concentrations of LiTFSI relative to the LHP NCs, such as 0.1, 1, 9, and 50 wt %. Thin films have been prepared by spin-coating under an inert atmosphere using these LiTFSI:NC mixed solutions, and their properties were compared with corresponding thin films made from the native NC solutions. In the following, we focus on green CsPbBr<sub>3</sub>NCs; blue and red NCs are only discussed in the LED part of this manuscript, but we anticipate that they behave qualitatively similar regarding the effect of LiTFSI on optical, electronic, and charge transport behavior. We mostly consider the 1 wt % LiTFSI doped thin films for characterization, because PeLEDs with this LiTFSI content show the highest luminance while being close to the optimal efficiency, as will be discussed later.

In general, film formation without and with LiTFSI is found to be very similar (see Figure S5) so that we will not discuss this in detail here. CsPbBr<sub>3</sub> NCs of size 7–8 nm arrange in a cubic packing of the NCs on the surface of various kinds of substrates. We do not find a significant difference in NC arrangement and coverage, indicating that the addition of LiTFSI to the NC solutions preserves a certain fraction of the native oleylamine and oleic acid ligands, as schematically shown in Figure 1. It is important to note that we do not see a significant shrinkage of the NC size upon LiTFSI treatment, in contrast to the findings of Liu et al., where they observe etching of the NC surface by the acidic (H)TFSI.<sup>25</sup> These films were subsequently studied by photoluminescence, photoelectron spectroscopy, density functional theory modeling, and in PeLEDs.

Arguments for successful ligand exchange come from changes of photoluminescence (PL) spectra and lifetimes as well as from photoelectron spectroscopy, as will be discussed in the following two sections.

**2.2. Photoluminescence.** Photoluminescence spectra, quantum yield (PLQY), and lifetime are key indicators for the structural intactness of the LHP NC surfaces, both in solution as well as in thin films. Thereby, not only does ligand passivation play a key role but also the dielectric environment and the substrate on which the NCs are deposited. Figure 2 shows a comparison of PLQY of native, i.e., oleylamine/oleic acid-capped, CsPbBr<sub>3</sub> NCs on various substrates relative to glass (BK7). When using highly conductive substrates like metals, ITO, ZnO, or PEDOT:PSS, the PLQY is significantly lowered compared with glass. For PEDOT:PSS, the quantum yield reduction can be ascribed to residual water content, which may degrade the LHP NC significantly and quench luminescence.<sup>26,27</sup> The reduction for ZnO and ITO however originates from a different mechanism; e.g., their high carrier densities may enable exciton-carrier quenching or the oxides could lead to degradation of the LHPs.<sup>28</sup> And even in the case of the organic polymer polyvinylcarbazole (PVK), used as hole transporting layer (HTL) in PeLEDs, the PLQY is slightly lowered with respect to glass. However, by introducing LiTFSI as dopant in PVK the impairment is overcome. LiTFSI as dopant in HTLs is reported to increase their electrical conductivity rendering this effect rather unexpected.<sup>29</sup> Another Li-based substrate treatment is a thin film of LiF evaporated on glass before spin-coating of the LHP NCs, which proves to be even more beneficial on the PLQY (see Figure 2a). A positive effect of an LiF interlayer has already been observed for light emission from bulk perovskites. Bigger grain sizes and reduced pinholes in the film were identified as the main cause for a better optical performance.<sup>30</sup> For LHP NCs the grain sizes are

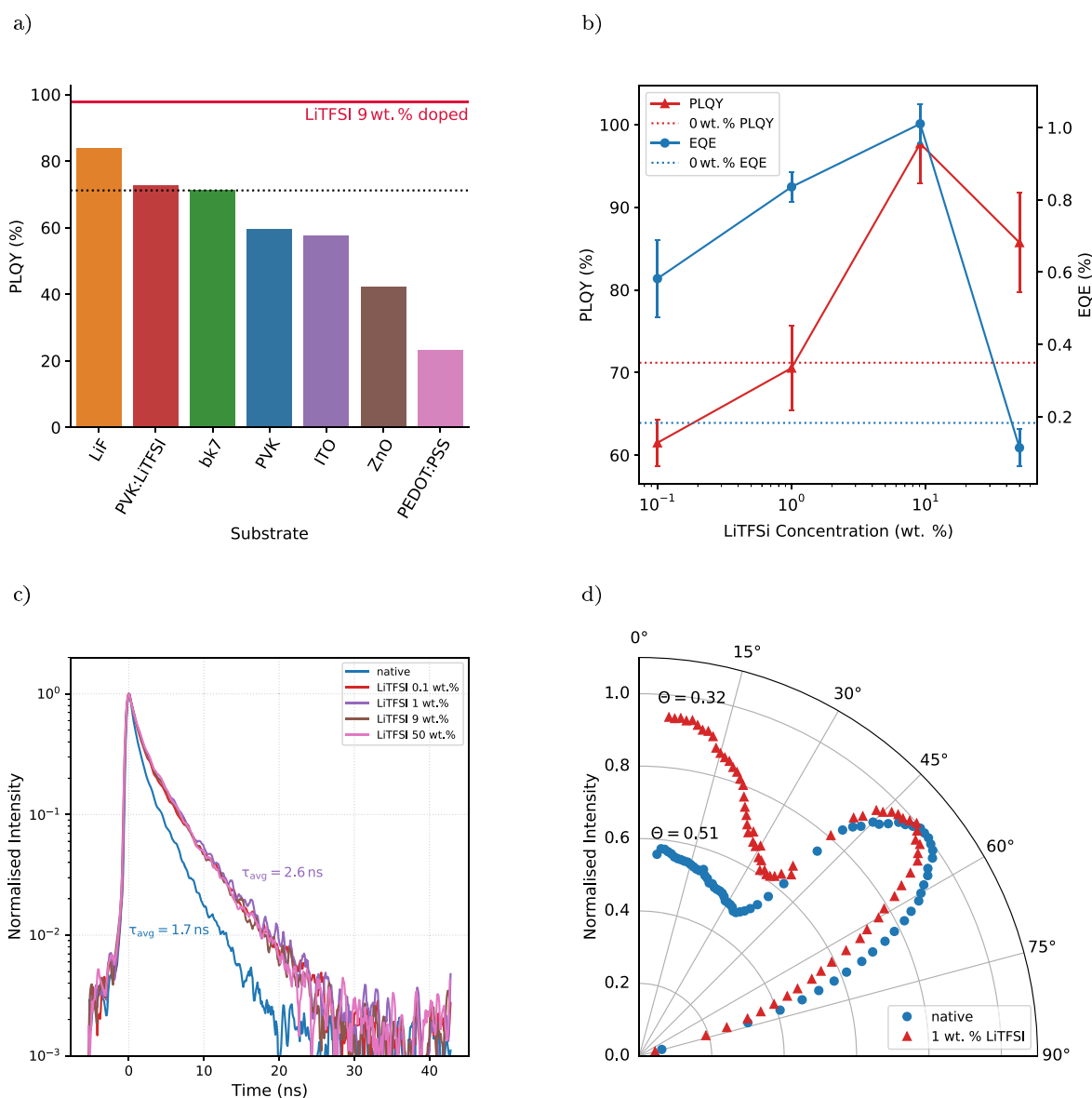


**Figure 2.** (a) PLQY of CsPbBr<sub>3</sub> NC thin films on various substrates; (b) LiTFSI doping concentration dependent PLQY and EQE; (c) TRPL decay curves; (d) p-polarized ADPL spectra.

predefined during synthesis and not expected to change upon spin-coating on a substrate.<sup>11</sup> Consequently, it is reasonable to assume a different mechanism for the PLQY enhancement.

This raises the question, whether the nature of the substrate alone affects the PLQY, or if there is interdiffusion from the underlying material into the LHP NC thin film. Thus, to study the influence of LiTFSI on the CsPbBr<sub>3</sub> NCs, we directly add the Li salt to the solution prior to spin-coating on glass. Even though a more polar solvent, viz. chlorobenzene, is needed to mix the two substances, an increase in PLQY can be observed, both, in solution and as a thin film. Figure 2b shows the PLQYs of thin-films fabricated with different LiTFSI mass percentage mixing ratios. At very low concentrations, the PLQY is slightly decreased with respect to the pristine (0 wt %) LHP NC film, which has a PLQY of about 70%. In contrast to that, at concentrations higher than 1 wt %, the PLQY is significantly increased reaching near unity at 9 wt %, before it decreases again for a 1:1 mixture of both components. The PLQY impairment at low concentrations is comparable to a

solvent mixture of toluene and chlorobenzene (but no LiTFSI), which may imply that some of the NCs are irreversibly degraded by the polar solvent before this detrimental effect is outweighed at higher LiTFSI content.<sup>31</sup>

Together with the changes in the PLQY of LiTFSI-treated CsPbBr<sub>3</sub> NC films, we also observed a slight red shift of their PL emission spectra (Figure S1), which is indicative of ligand exchange by the addition of LiTFSI to the NC solutions prior to spin-coating. Similar observations were recently reported on red-emitting LHP NC and were assigned to the highly dynamic/labile binding situation of oleic acid and oleylamine on the perovskite NC surface.<sup>32,33</sup> Therefore, both the enhanced PLQY and the spectral PL red shift indicate that the new ligand must be in spatial proximity to the NC surface, which is only possible if the native ligand (oleic acid/oleylamine) is replaced.

Because we assumed a surface trap passivation effect by the LiTFSI, time-resolved photoluminescence (TRPL) was measured on the same films (Figure 2c). As detailed in the

Supporting Information (Figures S2 and S3), the PL transients show a double-exponential decay with a fast initial lifetime of about 1 ns and a slower one with several nanoseconds. Weighting the lifetimes with their relative amplitudes, one obtains an average lifetime, as explained in the context of Figures S2 and S3. For the native sample  $\tau_{\text{avg}} = 1.7$  ns is obtained, whereas all the LiTFSI-doped ones have similar  $\tau_{\text{avg}} = 2.6$  ns, with only minor variation  $\Delta\tau_{\text{avg}} = 0.1$  ns (see Figure 2c), which is surprising in view of the observed changes in the PLQY over the same concentration range. However, as discussed above, the PLQY is reduced if there are solvent-degraded LHP NCs in the film, which contribute to absorption of the incident UV light but not to light emission in the visible range. On the other hand, the PL lifetimes do not necessarily have to be affected by degraded LHP NC; if they do not interact with the optically active ones, the obtained lifetimes originate only from intact NCs because the degraded ones are not detected, in contrast to the PLQY measurement.

As the double-exponential fits on the intensity decay (see Figure S2 and S3) reveal, the individual PL lifetimes are concentration independent (just like the average,  $\tau_{\text{avg}}$ ). However, a comparison of the amplitudes exhibits a shift of weights toward the longer lifetime with increasing LiTFSI concentration. Together with the PLQY measurements, this implies that within the short lifetime there are more nonradiative decay processes. Furthermore, this could indicate that trap-assisted recombination is suppressed by the presence of LiTFSI. There have been several reports about surface trap passivation featuring various halide salts. They agree on a passivation mechanism by halide abundance, which has also been reported by groups using lithium-free halide salts.<sup>34–37</sup> However, in our case, the halide-free LiTFSI seems to have a similar effect.

In addition to the changes in PLQY and PL lifetime, we observe a change of the radiation pattern of LHP NC films upon addition of LiTFSI. Figure 2d shows the parallelly polarized (p-pol.) angular dependent photoluminescence (ADPL) of a native and a 1 wt % LiTFSI-treated CsPbBr<sub>3</sub> NC thin film. As studied in great detail for organic light emitters<sup>38</sup> as well as for some LHP NCs,<sup>39,40</sup> such radiation patterns contain information about the average orientation of the transition dipole moments (TDM) of the electronically active optical transition from the excited state to the ground state. This parameter is key to understanding and improving light outcoupling from thin-film light-emitting structures, such as organic LEDs<sup>38</sup> or PeLEDs.<sup>41</sup> In particular, the orientation parameter  $\Theta$  (which is defined as the fraction of power emitted by vertical TDMs) directly indicates the degree of anisotropy of the TDM orientation distribution, with  $\Theta = 0.33$  being the isotropic case, and larger (smaller) values indicating more vertical (horizontal) TDM orientation. By comparing native CsPbBr<sub>3</sub> and LiTFSI-treated NCs we notice a significant change of the TDM orientation. After fitting with an appropriate dipole model (details in the Supporting Information) a TDM orientation parameter of  $\Theta_{\text{native}} = 0.51$  is obtained, proving more vertical TDM orientation for the native NCs, in contrast to  $\Theta_{\text{LiTFSI}} = 0.32$  being close to isotropic for the 1 wt % LiTFSI-treated NCs. This means that the unfavorable vertical TDM orientation of the native NC film is changed to an isotropic emission profile corresponding to the cubic structure of LHP. A similar behavior has also been found by an Al<sub>2</sub>O<sub>3</sub> overcoating of LHP nanoplatelets.<sup>39,42</sup> Thus, we suppose that LiTFSI acts as a dielectric layer to

screen the asymmetry in the electrostatics between the substrate and the free surface of the NCs.

**2.3. Energy Level Alignment.** To elucidate the impact of LiTFSI on the electronic properties of LHP NCs, ultraviolet and X-ray photoelectron spectroscopy (UPS and XPS) measurements have been conducted on the PVK/CsPbBr<sub>3</sub>-NC and PVK/CsPbBr<sub>3</sub>-NC:LiTFSI films, respectively. As shown in Figure 3a by the valence region and the secondary electron cutoff spectra, the PVK film exhibits an initial work

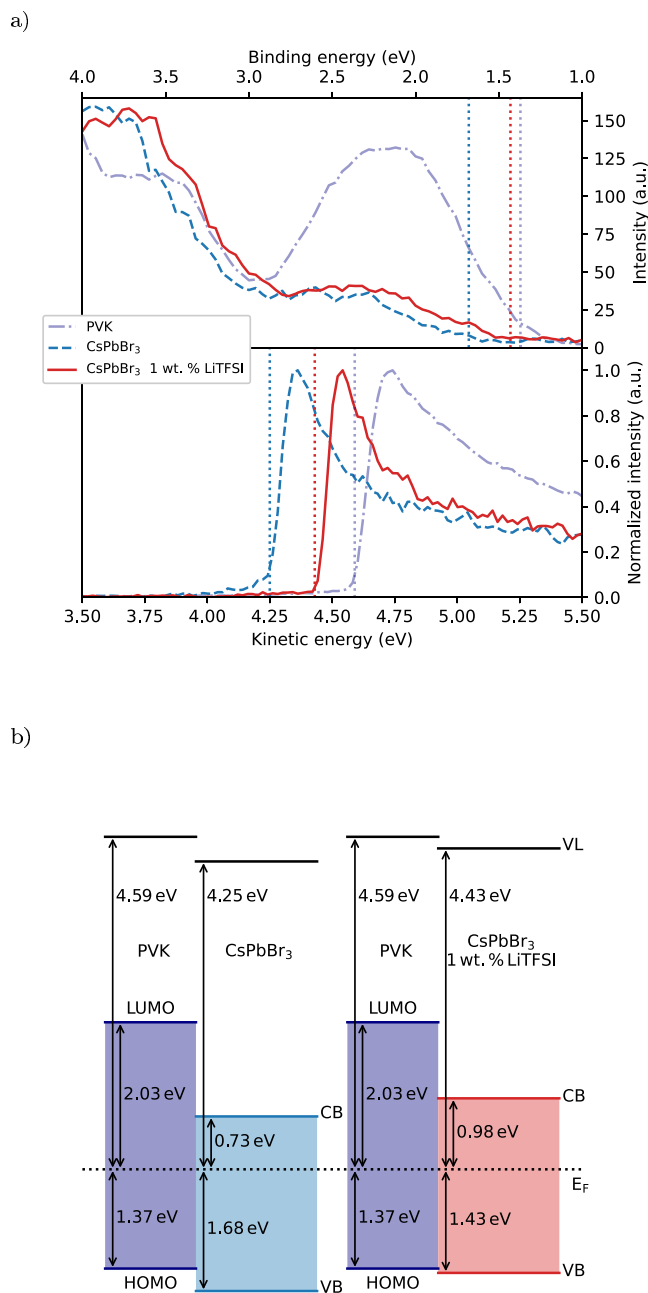


**Figure 3.** (a) UPS spectra of PVK and PVK/CsPbBr<sub>3</sub>-NC films with and without the addition of LiTFSI. Top panel, valence band spectra; bottom panel, secondary electron cutoff region. (b) Energy level diagram at the PVK/CsPbBr<sub>3</sub> interface with and without addition of LiTFSI. VL and  $E_{\text{F}}$  refer to vacuum level and Fermi level (set at 0 eV binding energy). Bandgaps are taken from the optical gap for the perovskite and from literature for PVK.<sup>43</sup>

function of 4.59 eV and the highest occupied molecular orbital (HOMO) level is found at 1.37 eV binding energy (with respect to  $E_F$ ). Upon deposition of CsPbBr<sub>3</sub> NCs, the work function decreases to 4.25 eV, likely due to the formation of band bending and/or an interface dipole at the buried interface.<sup>44</sup> The valence band (VB) onset of CsPbBr<sub>3</sub> is then extrapolated at 1.68 eV with respect to  $E_F$ . Given the energy gap of CsPbBr<sub>3</sub> of about 2.4 eV (515 nm), this shows that  $E_F$  is located above midgap which is due to a strong n-type character on the surface of the NCs. Additional surface photovoltage measurements under white light illumination shows no shifts of CsPbBr<sub>3</sub> NC energy levels, indicating a flat band condition through the LHP NC layer.<sup>45</sup> Hence, the surface energy levels are then expected to also reflect the electronic properties within the LHP NC thin-film. With the addition of LiTFSI to the CsPbBr<sub>3</sub> NCs, a shift of the valence band toward lower binding energy by 0.25 eV is observed, which is accompanied by an increase in sample work function, leading to a decrease in VB onset to 1.43 eV with respect to  $E_F$ .

A similar shift of the core levels was observed in XPS (see Figure S6). Such a rigid shift of all CsPbBr<sub>3</sub>-NC energy levels distinctly demonstrates a p-doping effect by the addition of LiTFSI. It is worth mentioning that the use of substantially attenuated UV flux (attenuation of more than 100 times compared to the standard helium discharge lamp) is required for the UPS measurement, as a high UV flux is found to cause irreversible changes of the electronic structure. However, this leads to insufficient signal-to-noise ratio at the top VB region, which keeps us from extracting the LHP NC valence band onset on a logarithmic intensity scale of the photoelectron signal, as is known to accurately infer the band edge position of perovskite films due to the low density of states at the top of the valence band.<sup>46,47</sup> However, the shift of the electronic levels is not affected by this procedure.

Furthermore, XPS can serve as another proof for successful ligand exchange. Similar to Liu et al., we find a fluorine peak (F 1s) in the XPS spectrum of the LiTFSI-treated NC film (see Figure S6d), which could not be observed in the native sample.<sup>25</sup> However, because of the low X-ray intensity used in our experiments, nitrogen and sulfur peaks could not be identified. Nevertheless, following the consideration of Liu et al., it can be concluded that TFSI<sup>-</sup> is attached at the surface of the NCs.<sup>25</sup>

The resulting energy level diagram of the PVK/CsPbBr<sub>3</sub> NC stack is shown in Figure 3b. It can be clearly seen that the PVK/CsPbBr<sub>3</sub>-NC interface initially exhibits a large energy barrier of ca. 0.31 eV for hole injection. Because of the p-doping effect by addition of LiTFSI, such an energy barrier is reduced to 0.06 eV with CsPbBr<sub>3</sub> NC VB edge shifting closer to the HOMO level of PVK. With such reduction, the hole injection can be significantly improved.

The reduced hole injection barrier is manifested in the electrical transport behavior as well. As expected, a single carrier hole-only device (layer stack shown in the inset of Figure 4) with 1% LiTFSI doping shows a significant increase, respectively doubles the current density when operated at 4 V (see Figure 4). We note that this current enhancement is not caused by a change in the layer morphology (including its thickness). As shown in the Supporting Information (Figure S5), both native and LiTFSI-treated CsPbBr<sub>3</sub>-NC films have similar morphology with a partially closed uppermost NC monolayer on top of fully closed layer(s) underneath. If at all, the LiTFSI treatment even slightly improves the film

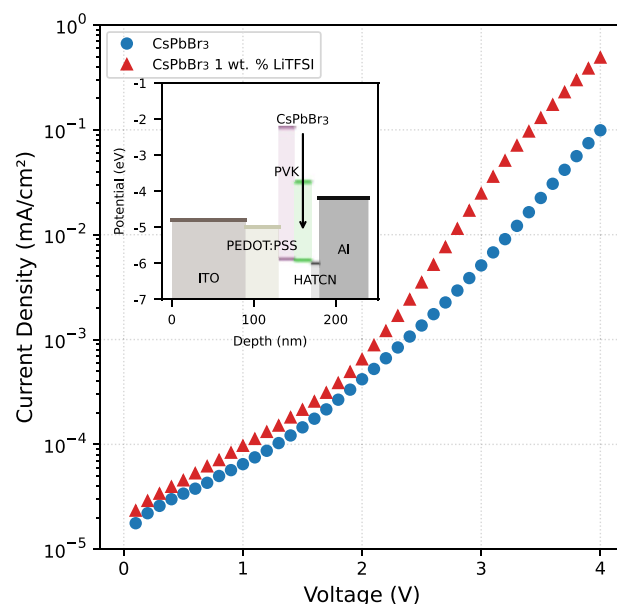


Figure 4. Hole-only  $j$ - $V$  curve with the schematic device stack as inset.

morphology so that the increase of current cannot originate from insufficient NC coverage. Further, one can also expect to obtain different electronic coupling among the CsPbBr<sub>3</sub> NCs by replacing (part of) the insulating oleylamine/oleic acid ligands by LiTFSI so that an improved bulk charge transport might also contribute to the observed current enhancement. We also note that electron injection is apparently not affected by the energy level shift, as electron-only devices (see Figure S7d) show a negligible difference in current.

**2.4. Density Functional Theory Modeling.** Density functional theory (DFT) modeling of four slab models was performed (see the Supporting Information for computational details) to understand the structural changes upon LiTFSI treatment and its consequent impact on the electronic structure of the CsPbBr<sub>3</sub> NCs. As shown in Figure 5a, model A consists of pristine CsPbBr<sub>3</sub>, whereas in model B, a Li<sup>+</sup> ion replaces a Cs<sup>+</sup> ion together with a TFSI<sup>-</sup> replacing a Br<sup>-</sup> ion over the surface. Model C considers intercalation of a Li<sup>+</sup> ion, with one TFSI<sup>-</sup> placed over the CsBr-terminated surface, whereas model D is a system analogous to model C, but with the two -CF<sub>3</sub> groups of the TFSI<sup>-</sup> ion having been replaced with two -CH<sub>3</sub> groups.

Even though model D is not relevant experimentally, we explored this system computationally to disentangle the effect of C-F bond polarity on work function (WF), by closely comparing it with its C-H analogue.

We found that both pristine and LiTFSI-doped systems exhibit a very similar density of states (Figure 5b), and the orbital contributions from the TFSI<sup>-</sup> ions are quite deep-lying, appearing only near -2.0 eV. On the other hand, the TFSI<sup>-</sup> ligands were found to alter the surface dipole moment of the particle significantly, causing a substantial shift in the vacuum level (Figure 5c). Consequently, the mere presence of a surface TFSI<sup>-</sup> ion in model B replacing a Br<sup>-</sup> ion increased the work function of the NC from 4.51 eV in pristine model A to 5.54 eV in model B. The vacuum level-shift is even more prominent in model C, partly attributable to the fact that the dipoles caused by the surface TFSI<sup>-</sup> ions are now exclusively outside the inorganic core, as opposed to model B, where the O atom

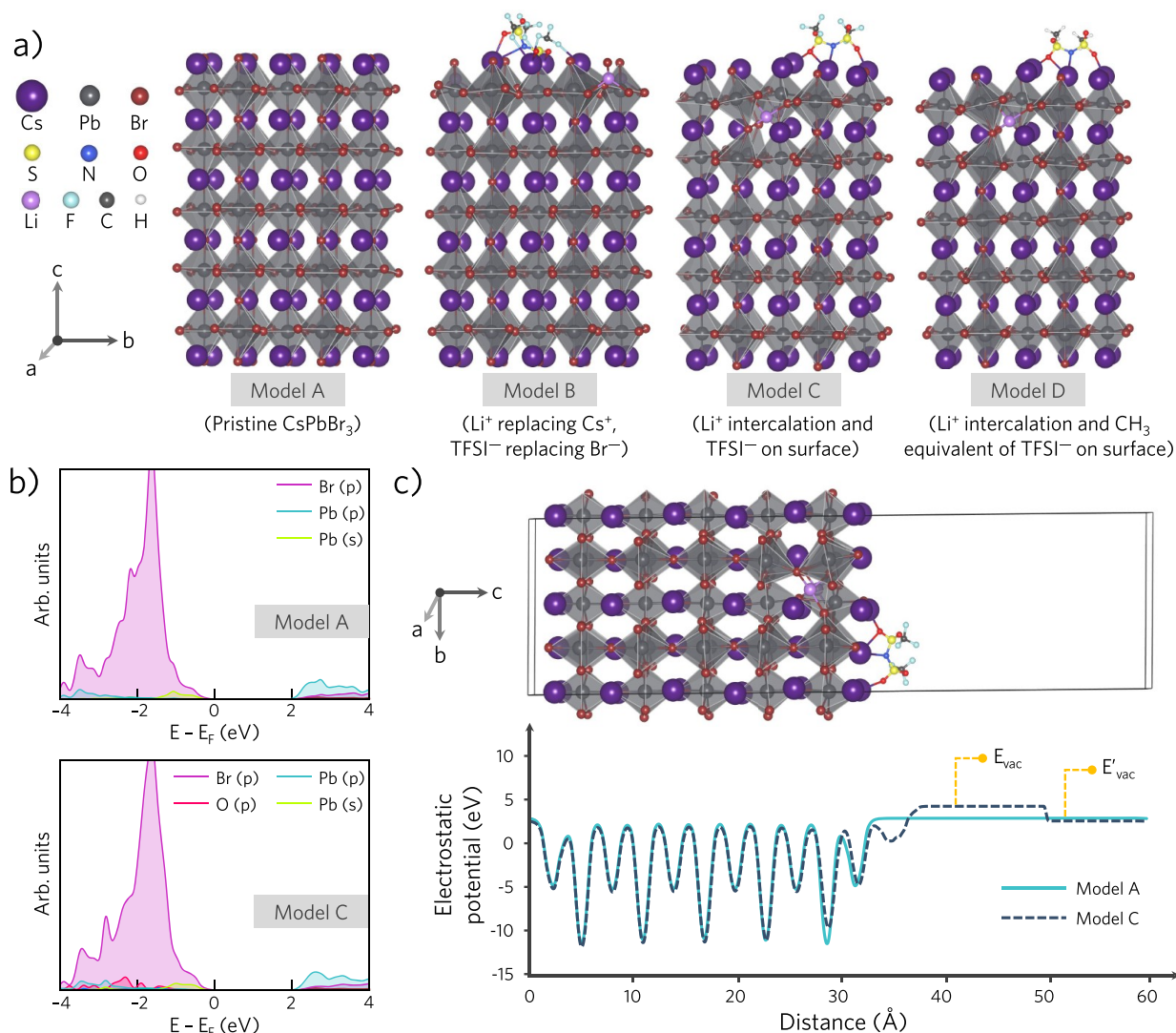


**Figure 5.** (a) Slab models of orthorhombic CsPbBr<sub>3</sub> (1 × 2 × 3 supercell; 5 Pbl layers) exposing the CsBr-terminated surfaces, (b) projected density of states plots for model A and C ( $E_F$  = Fermi energy), (c) planar average electrostatic potential for determining the vacuum energy level,  $E_{vac}$ . In the diagram,  $E_{vac}$  corresponds to the (near) vacuum level of the TFSI-deposited surface and  $E'_{vac}$  represents the undoped (far) vacuum level.

from TFSI binds to a Pb<sup>2+</sup> ion from the core and hence, the dipole is partly compensated. In model D, we show that when the highly polar C–F bonds in TFSI are replaced with C–H bonds, the vacuum level shift is drastically reduced ( $E_{vac} = 4.23$  eV and WF = 6.20 eV for –CF<sub>3</sub> groups in model C vs  $E_{vac} = 3.83$  eV and WF = 5.69 eV for –CH<sub>3</sub> groups in model D). We recognize that the computed change in the work function is rather substantial compared to the experiment (UPS measured hole stabilization being around 0.25 eV, Figure 3b). We attribute this discrepancy to (i) a higher TFSI<sup>–</sup> coverage in the model system compared to the experiment and (ii) the fact that in the slab model only one surface is asymmetrically covered with organic ligand as opposed to all six-side coverage in an actual NC.

In addition to the change in work function, the topotactic intercalation of the Li<sup>+</sup> ion, regardless of whether in a tetrahedral or octahedral site, has been demonstrated to increase interaction with neighboring halide ions (see Li–Br bonding in addition to the usual Cs–Br bonds in model C and D in Figure 5a),<sup>21</sup> and thus the activation barrier for halide ion migration is expected to increase.<sup>48</sup> We anticipate a similar

effect of the Li<sup>+</sup> ion on preventing ion migration and improving the structural integrity of the LiTFSI-treated CsPbBr<sub>3</sub> particles. Finally, we speculate that the availability of electronegative O atoms from the TFSI<sup>–</sup> ligand, which is quite mobile over the surface, would also coordinate to Pb atoms, as seen in model B, and contribute toward preventing detrimental Pb<sup>2+</sup> to Pb<sup>0</sup> reduction over the surface.<sup>49</sup>

**2.5. Perovskite Light-Emitting Diodes.** Finally, we have employed native and LiTFSI-treated CsPbBr<sub>3</sub> NCs in PeLEDs, where PVK is used as polymeric hole transport layer and B3PYMPM as electron transport layer, followed by a LiF/Al cathode as depicted in the inset of Figure 6a, the corresponding current–voltage–luminance characteristics is also shown in Figure 6a. The native CsPbBr<sub>3</sub> NCs show two onsets for the current, with the first occurring slightly above 1 V which can be assigned to electrons due to the n-type position of the Fermi level; the second onset with a much steeper increase of current is located at about 3.5 V and would accordingly correspond to the onset of hole injection. This is supported by the fact that detectable luminance (>1 × 10<sup>–2</sup> cd/m<sup>2</sup>) occurs not before the applied voltage exceeds 4 V.

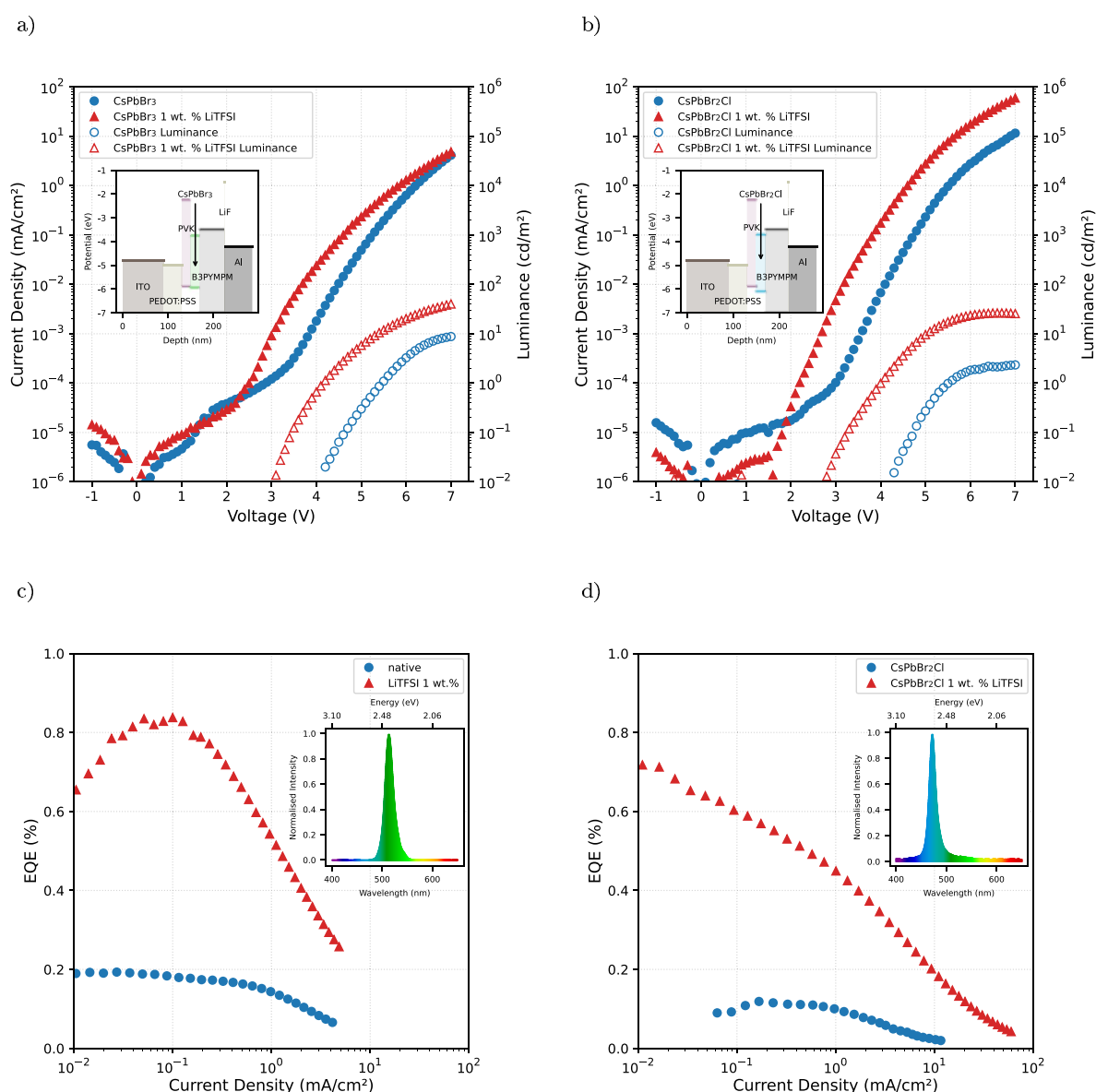


**Figure 6.**  $j$ - $V$ - $L$  curves of (a) CsPbBr<sub>3</sub> and (b) CsPbBr<sub>2</sub>Cl PeLEDs with and without LiTFSI-doping; (c, d) corresponding EQE vs current density curves. The insets depict their stack structures and their emission spectra.

For the 1 wt % LiTFSI-doped NCs, the double-step feature in the current disappears; rather, there is a steep increase starting above 2 V and luminance is detected already at 3 V. With further increasing voltage, both current and luminance increase much steeper in the LiTFSI-doped PeLED as compared to the untreated one. Finally, at 7 V both devices reach the same current, but the luminance in the LiTFSI-doped PeLED stays several times above the native one, indicating higher external quantum efficiency (EQE). This is shown in Figure 6c where the maximum EQE increases by more than a factor of 4 from 0.2% to above 0.8%. We also note that both, native and LiTFSI-treated CsPbBr<sub>3</sub>, PeLEDs have the same narrow green electroluminescence spectrum shown in the inset of Figure 6c.

Similar to the PLQY series, we have also fabricated PeLEDs with other LiTFSI doping concentrations (see Figure S7). We find that the highest EQE is reached for a LiTFSI concentration of 5 wt %; however, this device (just like the 9 wt %) does not reach the same level of luminance as the 1 wt

% device, indicating some kind of overdoping by LiTFSI that leads to irreversible device degradation at high current densities, while lower concentrations lack sufficiently high PLQY.

As a proof of concept, we also applied LiTFSI doping to sky-blue emitting CsPbBr<sub>2</sub>Cl NCs (results shown in Figure 6b, d). In this case, the reduction of the turn-on voltages for current and luminance induced by LiTFSI doping is even bigger, as detectable luminance sets in already below 3 V. The EQE is enhanced by a factor 7 from 0.1 to 0.7%, proving an even stronger effect of LiTFSI doping in the wider band gap, sky-blue PeLEDs.

Furthermore, a red methylammonium-PbBrI<sub>2</sub> NC PeLED can also be improved by LiTFSI, without an evident current-density increase (see Figure S8). In this case, the red NC emitter does not face the same hole injection barriers as its blue and green counterparts, such that an increase in hole-injection is not expected to play a major role. Nevertheless, the

device EQE is boosted by a similar factor through the LiTFSI treatment.

**2.6. Discussion.** The overall increase in PeLED performance with various LHP species implies a very versatile mechanism. The increase in PLQY and exciton lifetime with the LiTFSI concentration suggests a surface passivation mechanism. This has already been reported with lithium halides, where the lithium ions as well as the halides have shown surface trap passivation.<sup>20,21,50</sup> However, the influence of Li<sup>+</sup> has not been completely disentangled from that of the halide. Here we use the organic TFSI<sup>-</sup> anion, proving that a halide-free passivation is possible. As sulfonic moieties have been reported to fill halide vacancies, a similar interaction from LiTFSI seems plausible and has already been reported.<sup>10,25,51</sup> In particular, TFSI<sup>-</sup> has been suggested to act as surface passivation by coordinating with Pb and Cs cations on the NC surface. Additionally, suppressed hysteresis of the *j*-*V* characteristics (see Figure S7c) implies that ions have been demobilized to some extent. Although neither a significant shrinkage of the NCs nor a spectral blue-shift has been observed, as reported by Liu et al. upon (H)TFSI treatment,<sup>25</sup> an analogous chemical reaction may still take place on the NC surface: CsPbBr<sub>3</sub> + LiTFSI → CsPbBr<sub>2</sub>TFSI + LiBr. The main difference to the (H)TFSI passivation is that the resulting lithium halide salt is not as volatile as the corresponding halide acid (HBr in this case), effectively blocking a prolonged decomposition of the NC surface, thus avoiding shrinkage. Br<sup>-</sup> having a higher affinity to bind Li<sup>+</sup> than TFSI<sup>-</sup> renders this process energetically favorable.<sup>52</sup> This could explain why the addition of LiTFSI passivates CsPbBr<sub>3</sub> NCs without degrading their shape and size. Apart from that, an enhanced stability to polar solvents as reported by Liu et al. is also exhibited by our LiTFSI-treated NCs.<sup>25</sup>

Though, upon considering the PLQY and EQE depending on LiTFSI concentration (Figure 2 b) it becomes evident, that apart from surface trap passivation another beneficial consequence arises from the LiTFSI treatment. The different dependence on LiTFSI concentration between EQE and PLQY cannot fully be explained by a surface trap passivation mechanism, because the EQE ( $\eta_{\text{EQE}}$ ) is proportional to the PLQY:

$$\eta_{\text{EQE}} = \eta_{\text{out}} q_{\text{PLQY}} \gamma \quad (1)$$

However, at small doping concentrations the drop in EQE is not as pronounced as it is for the PLQY. Other factors only influencing the EQE are the outcoupling factor ( $\eta_{\text{out}}$ ) and the charge carrier balance ( $\gamma$ ).<sup>38</sup> So an emitter orientation change can enhance the EQE compared to the PLQY, by a limited amount. This change in radiation pattern is observed as shown in Figure 2d, but the change of orientation is simulated to result in an EQE increase factor of only 1.3. Considering the PeLED fabricated with a 1 wt % LiTFSI doping, as compared to the one with native CsPbBr<sub>3</sub> NCs, the PLQY does not change significantly but the EQE does from about 0.2 to 0.8% by a factor of 4. The orientation alone cannot account for such large enhancement, but the last factor, the charge carrier balance can. Consequently, the doping procedure modifies the charge carrier balance in favor of EQE. Further investigations into that have been made by designing a hole-only device. This device exhibits hole-currents up to a factor 6 higher for the doped sample (see Figure 4), implying an increased hole injection of roughly the same factor. The leveraged hole-injection can be ascribed to an improved VB alignment with

the adjacent PVK's HOMO level, as measured by UPS and XPS (see Figure 3). The injection barrier is reduced from 0.31 to 0.06 eV, which is in accordance with the increased hole current in the devices. At that, not only the VB onset is shifted but the entire density of states by 0.25 eV, raising the CB level by the same amount and rendering the CsPbBr<sub>3</sub>-NC semiconducting thin film less n-type.

This energy-level shift is expected when considering the reports of using LiTFSI as a p-dopant in organic semiconductors. In that case, oxygen plays a key role in enabling the doping process, which is proven by lithium oxide residuals after successful doping.<sup>53,54</sup> Even though the LiTFSI treatment here is realized in the absence of oxygen, a comparable reaction may lead to p-doping of the NCs. However, direct signatures of charge transfer could not be found in photoelectron spectroscopy, which is understandable, as these NC films have a very large surface area-to-volume ratio, making the detection of new electronic states upon charge transfer hard. Nevertheless, the observed rigid shift of all energy levels (including the core levels) clearly proves p-doping upon LiTFSI treatment of the CsPbBr<sub>3</sub>NCs.

The significance of the VB alignment can be seen when comparing the differently colored LEDs: For the blue CsPbBr<sub>2</sub>Cl, the enhancement of current and EQE is highest, it decreases in green CsPbBr<sub>3</sub> to no significant current increase for the red MAPbBr<sub>2</sub>I<sub>2</sub>. The sky-blue CsPbBr<sub>2</sub>Cl has a VB onset reported to be even lower,<sup>55</sup> rendering a potential p-doping even more beneficial as observed. The red device presumably does not benefit by the energy level shift, because of its small bandgap<sup>55</sup> the injection barrier has not been the limiting factor, even though the EQE is still significantly increased.

When considering the higher doping concentrations, 5 wt % and more, a drop in luminance at elevated currents can be observed (see Figure S7a, b). Although the currents are further increasing, the luminance does not exceed 20 cd/m<sup>2</sup>. A drastic EQE drop occurs at this critical luminance value. This drop is proven to be irreversible by multiple measurement runs of the LEDs. Apparently, there is a degradation induced by an excess of LiTFSI doping. Different interactions of lithium ions with the LHP NCs ranging from residing on an interstitial position over cation exchange (Cs<sup>+</sup> for CsPbBr<sub>3</sub>) to filling lead vacancies have been explored.<sup>21</sup> Upon excess doping multiple of these interactions may mix and change the LHP NCs properties toward lower stability and quantum yields. Even though this drop in quantum yield is observed in PLQY measurements at 50 wt % doping only, the drop in operational stability is already dominant for the PeLEDs starting from 5 wt %. The degradation above a certain luminance together with the fact that CsPbBr<sub>3</sub> is optically stable even upon strong excitations<sup>56,57</sup> leads to the conclusion that the degradation has to originate from an interaction between charge carriers and the excited state. Because of the revealed n-type nature of the LHP NCs and the different current onsets observed in the *j*-*V*-*L* curves, it is evident that there is an electron abundance in the device during light-emission. Several reports suggest a chemical reduction reaction of lead as a major degradation path in LHPs,<sup>58,59</sup> which may be facilitated by this surplus of electrons in PeLEDs during operation. Finally the trion state, consisting of two electrons and one hole, may be the main cause of degradation. LiTFSI seems to have no influence on this proposed electron-induced degradation, because it plays only a minor role in the mitigation of electrons, if at all. Its major contribution is ascribed to the easier hole injection into

the LHP NCs not necessarily caused by the slightly less n-type energy alignment but rather by the reduced hole injection barrier. As a consequence, the degradation seems to affect the EQE in PeLEDs significantly. With the red and blue device, the LiTFSI has proven to be very versatile, increasing the performance of simple all-inorganic tribromide LHP NCs as well as mixed halide or organic perovskite NCs. However, the degradation of PeLEDs cannot be prevented by the use of LiTFSI, because its major influence is related to hole injection and increased PL quantum efficiency.

### 3. CONCLUSION

Surface defect passivation has already been recognized as key to enhance the performance of LHP NCs regarding its optoelectronic properties. Here we investigate surface treatment with a p-dopant, viz. the organic lithium salt LiTFSI, and show that the efficiency in PeLEDs is tremendously enhanced. We trace this enhancement back to positive effects on three decisive properties considering their EQE: the emitter's quantum yield is proven to be brought close to unity. This is achieved by most surface passivation techniques on LHP NCs. Additionally, the angular emission pattern is changed in favor of better light outcoupling. Although these two effects contribute to the increased efficiency to a certain extent, the most pronounced influence is identified to be the simultaneous tuning of the charge carrier balance to promote hole injection. Enhancement in these three key factors is a remarkable feature that can be attributed to the LiTFSI treatment. However, there are still challenges concerning stability, which is a major issue for LHP NCs in LEDs in general. At the same time the interaction as well as degradation of LHP NCs in conjunction with LiTFSI is not entirely understood. Nevertheless, a 4–7 fold increase in EQE can be achieved for PeLEDs of various colors and chemistry, rendering the LiTFSI treatment a very promising procedure to further investigate.

### 4. METHODS

**4.1. Materials.** ITO (indium tin oxide) substrates with dimensions  $2 \times 2$  cm were purchased by Kintec (Hong Kong) with and without a custom layer thickness pattern of 100 nm on a 23 nm  $\text{SiO}_2$  buffer on a 0.7 mm thick glass substrate. Fused silica ( $\text{SiO}_2$ ) substrates with dimensions  $2 \times 2$  cm with a thickness of 0.7 mm were bought from Nano Quarz Wafer Germany GmbH. PEDOT:PSS in a low-conductive ratio of 1:20 was used, having the descriptor CH8000, by Heraeus Germany GmbH & Co. KG. ZnO was synthesized from zinc acetate using the sol–gel method.<sup>60</sup>  $\text{CsPbBr}_3$  solution ( $c = 10$  mg/mL in toluene, product ID 900746) and LiTFSI (Lithium bis(trifluoromethane)sulfonimide, 99.95% trace metal basis, product ID 544094) were ordered from Merck Germany KGaA. PVK (Poly(9-vinylcarbazole),  $M_w > 1 \times 10^5$ , product ID LT-N4078) was obtained from Luminescence Technology Corp. (Lumtec, Taiwan).

**4.2. Nanoparticle Preparation. Preparation of Oleylammonium Halide (OLA-HX).** To prepare a 1.1 mmol/mL OLA-HX precursor solution, we placed 10 mL of oleylamine (OAm) in a 25 mL three-neck flask and slowly added either 1 mL of concentrated hydrochloric acid ( $\text{HCl}_{(\text{aq})}$ ) or 1.28 mL of concentrated hydrobromic acid ( $\text{HBr}_{(\text{aq})}$ ). Subsequently, the solidified reaction mixture was heated at 120 °C under nitrogen atmosphere for 2 h. The reaction temperature has then been increased to 150 °C for 30 min and afterward allowed to cool to room temperature. The mixture was kept in a glovebox and heated to 80 °C before injection.

**$\text{CsPbBr}_2\text{Cl}$  Nanocrystals.**  $\text{CsPbBr}_2\text{Cl}$  nanocrystals were prepared by a hot-injection synthesis using a modified literature method.<sup>54</sup> To synthesize 7 nm  $\text{CsPbBr}_2\text{Cl}$  nanocrystals, 49 mg (0.15 mmol) of  $\text{Cs}_2\text{CO}_3$ , 67 mg (0.3 mmol) of PbO, and 1.5 mL of oleic acid (OA)

were degassed in 15 mL of ODE in a 50 mL three-neck flask under reduced pressure at 120 °C for 1 h. The temperature was increased to 240 °C under a nitrogen atmosphere, 1 mL of OLA-HBr and 0.5 mL of OLA-HCl precursor were quickly injected, and after 1 min, the reaction mixture was cooled to room temperature using an ice bath (below 180 °C).  $\text{CsPbBr}_2\text{Cl}$  NCs were collected by centrifuging the suspension (7000 rpm, 10 min.), decanting the supernatant, and collecting the precipitate. The precipitate was centrifuged again without the addition of a solvent (7000 rpm, 5 min.), and the resulting supernatant was removed with a syringe to separate the traces of residual supernatant. The precipitate was dissolved in 2 mL of hexane and centrifuged again (2500 rpm, 5 min) to remove aggregates and larger particles. The resulting supernatant was filtered through a 0.2  $\mu\text{m}$  PTFE syringe filter and stored as stock solution inside of a glovebox with a typical concentration of 25 mM following Maes et al.<sup>61</sup>

**LiTFSI Treatment.** The LiTFSI solution was diluted from a stock that was created by dissolving 200 mg of LiTFSI with 2 mL of dimethylformamide (DMF) and 18 mL of chlorobenzene (CB) by stirring overnight, resulting in a volume concentration of 10 mg/mL. Dilution to 1, 0.1, and 0.01 mg/mL concentrations was done with CB only.

Equal volumes of LHP NC solution and LiTFSI solutions were mixed to obtain a LiTFSI-doped solution. Mixing equal volumes of 10 mg/mL LHP NC and 10 mg/mL LiTFSI yielded a 5 mg/mL LHP NC solution with 50 wt % LiTFSI doping. Analogously, 9.09, 0.990, and 0.099 wt % doped solutions were obtained by using 1, 0.1, and 0.01 mg/mL concentrated LiTFSI solution and mixing with the 10 mg/mL LHP NC solution in equal volumes. All LHP NC solutions were created within a nitrogen-filled glovebox and exhibited stable luminescence for at least 3 months at room temperature.

**4.3. Sample Preparation. Photoluminescence.** Fused silica was used as a substrate for all PL measurements, that is PLQY, TRPL, and ADPL. The substrates were spin-coated in a nitrogen-filled glovebox by dropping 50  $\mu\text{L}$  (p.r.n. LiTFSI-doped) of LHP NC solution before starting the rotation of the spin-coater. After a settling time of 30 s, it was accelerated to 500 rpm and kept at that speed for another 30 s. To remove residuals from the edges, spinning for 5 s at 2000 rpm was applied before the procedure was stopped.

**UPS/XPS, SEM, LEDs, and Single-Carrier Devices.** For UPS/XPS and SEM, unpatterned ITO substrates were used, and for the electrical devices, patterned ITO substrates were used. For the electron-only device, a fused-silica substrate was smoothed with a 0.8  $\mu\text{m}$  thick PMMA layer before depositing 7.5 nm aluminum and 1 nm LiF as a bottom electrode. Initially, PEDOT:PSS was spin-coated in the cleanroom, at 4000 rpm for 30 s, and heated on a hot plate at 130 °C for 15 min, resulting in a smooth approximately 40 nm thin film. The samples were transferred to a nitrogen-filled glovebox immediately. As a second layer, the approximately 20 nm thin PVK film was deposited by spin-coating a 3 mg/mL concentrated PVK-chlorobenzene solution at 3000 rpm for 30 s and heating at 175 °C for 30 min. The LHP NC solutions are spin-coated as described for the PL samples, after cooling the substrate to room temperature, resulting in a closed film of about 2–3 monolayers (effective thickness approximately 20 nm).

The sample in the current state, that is, the bottom-half LED, was used for UPS/XPS and SEM investigations. For devices, the samples were transferred without ambient exposure into a high vacuum chamber, with a pressure less than  $1 \times 10^{-6}$  mbar. For the hole-only device, 10 nm HATCN (rate: 50 pm/s) was evaporated, and for LEDs and the electron-only device, 55 nm B3PYMPM (rate: 100 pm/s) followed by 0.5 nm LiF (rate: 10 pm/s) were evaporated. The devices were finished with a 60 nm (rate: 100 pm/s) thick aluminum cathode, also deposited by thermal deposition.

**4.4. Measurement Details. PLQY.** The PLQY was determined by a two-step method of measurement featuring a  $\text{BaSO}_4$ -coated integrating sphere.<sup>62</sup> The excitation source was a HeCd laser's 442 nm light. The excitation signal as well as the sample fluorescence was collected with a fiber and guided into a Princeton Instruments Acton2300i spectrometer, which was connected to a nitrogen-cooled

CCD camera (Princeton Instruments Pylon BRX100). An absolute calibration of the integrating-sphere CCD system was performed with a lamp calibrated for spectral irradiance according to the NIST standard by GigaHertz Optik GmbH Germany. With that system, spectra could be evaluated to its amount of photons and consequently a PLQY was calculated.

**ADPL.** The ADPL measurement and analysis were performed as previously reported by our group.<sup>41</sup> The spectrum was recorded with the same CCD spectrometer system as explained for the PLQY.

**TRPL.** Transient photoluminescence was recorded by the C5680 streak camera system by Hamamatsu, after being delayed by a Stanford Instruments DG535 while being spectrally analyzed by an Acton Spectra Pro 2300i. Excitation was done with the EKSPLA PT400 diode pumped solid-state laser set to wavelength 355 nm.

**UPS/XPS.** Ultraviolet photoelectron spectroscopy (UPS) measurements have been conducted using a SPECS PHOIBOS 100 hemispherical electron analyzer equipped with a monochromatized helium discharge lamp (21.22 eV). The UV flux was attenuated significantly by the monochromator to avoid UV-induced sample degradation. A sample bias of  $-10$  V was applied to acquire the secondary electron cutoff spectra. The base pressure of the analysis chamber has been kept below  $1 \times 10^{-9}$  mbar. X-ray photoelectron spectroscopy (XPS) measurements were performed at a JEOL JPS-9030 ultrahigh vacuum system (base pressure of  $1 \times 10^{-9}$  mbar) using monochromatized Al  $K_{\alpha}$  (1486.6 eV) radiation. Anode power of 30 W was applied for XPS measurements, which has not been found to induce noticeable sample degradation.

**LEDs and Hole-Only Devices.**  $j-V(-L)$  curves are recorded with a Keithley 2612B source meter unit (SMU). A photodiode of known diameter at known distance is used for luminance detection. The electroluminescent spectrum is taken with the Phelos system by Fluxim AG (Switzerland). With that and a Lambertian approximation, the EQE was determined. The integrity of the Lambertian approximation was ensured by random sampling with a calibrated integrating sphere (same setup as for PLQY). The sampling revealed that the photodiode's and consequently in this manuscript reported EQE was about 10% underestimated, relatively. For instance, the EQE of the 9 wt % LiTFSI-doped sample in Figure 2b showed 1.1% EQE in the integrating sphere, whereas it was 1% in the photodiode setup.

## ■ ASSOCIATED CONTENT

### SI Supporting Information

The Supporting Information is available free of charge at <https://pubs.acs.org/doi/10.1021/acsami.2c04018>.

PL spectra (Figure S1), TRPL fits and details (Figure S2 and S3), ADPL fits and details (Figure S4), SEM images (Figure S5), XPS spectra (Figure S6), details on DFT calculations with respective structures for the slab models, CsPbBr<sub>3</sub> NC LEDs at all LiTFSI concentrations, electron-only device (Figure S7), and MAPbBr<sub>2</sub> NC LED details (Figure S8); additional details on chemicals and preparation (PDF)

## ■ AUTHOR INFORMATION

### Corresponding Author

Wolfgang Brütting – Institut für Physik, Universität Augsburg, Augsburg 86135, Germany; [orcid.org/0000-0001-9895-8281](https://orcid.org/0000-0001-9895-8281); Email: [wolfgang.brueetting@physik.uni-augsburg.de](mailto:wolfgang.brueetting@physik.uni-augsburg.de)

### Authors

Tassilo Naujoks – Institut für Physik, Universität Augsburg, Augsburg 86135, Germany

Roshini Jayabalan – Institut für Physik, Universität Augsburg, Augsburg 86135, Germany

Christopher Kirsch – Institut für Physikalische und Theoretische Chemie, Universität Tübingen, Tübingen 72076, Germany

Fengshuo Zu – Institut für Physik & IRIS Adlershof, Humboldt-Universität zu Berlin, Berlin 12489, Germany

Mukunda Mandal – Max Planck Institute für Polymerforschung, Mainz 55128, Germany; [orcid.org/0000-0002-5984-465X](https://orcid.org/0000-0002-5984-465X)

Jan Wahl – Institut für Physikalische und Theoretische Chemie, Universität Tübingen, Tübingen 72076, Germany

Martin Waibel – Institut für Physik, Universität Augsburg, Augsburg 86135, Germany

Andreas Opitz – Institut für Physik & IRIS Adlershof, Humboldt-Universität zu Berlin, Berlin 12489, Germany; [orcid.org/0000-0002-3214-8398](https://orcid.org/0000-0002-3214-8398)

Norbert Koch – Institut für Physik & IRIS Adlershof, Humboldt-Universität zu Berlin, Berlin 12489, Germany; Helmholtz-Zentrum Berlin für Materialien und Energie GmbH, Berlin 12489, Germany; [orcid.org/0000-0002-6042-6447](https://orcid.org/0000-0002-6042-6447)

Denis Andrienko – Max Planck Institute für Polymerforschung, Mainz 55128, Germany; [orcid.org/0000-0002-1541-1377](https://orcid.org/0000-0002-1541-1377)

Marcus Scheele – Institut für Physikalische und Theoretische Chemie, Universität Tübingen, Tübingen 72076, Germany; [orcid.org/0000-0002-2704-3591](https://orcid.org/0000-0002-2704-3591)

Complete contact information is available at:

<https://pubs.acs.org/doi/10.1021/acsami.2c04018>

## Notes

The authors declare no competing financial interest.

## ■ ACKNOWLEDGMENTS

This work was funded by Deutsche Forschungsgemeinschaft (DFG) within Priority Program SPP2196 (“Perovskite Semiconductors: From Fundamental Properties to Devices”) under projects 424708673 and 423749265, as well as by their Heisenberg Program under grant SCHE1905/9-1. M.M. acknowledges postdoctoral support from the Alexander von Humboldt Foundation.

## ■ REFERENCES

- (1) Era, M.; Morimoto, S.; Tsutsui, T.; Saito, S. Organic-Inorganic Heterostructure Electroluminescent Device using a Layered Perovskite Semiconductor (C<sub>6</sub>H<sub>5</sub>C<sub>2</sub>H<sub>4</sub>NH<sub>3</sub>)<sub>2</sub>PbI<sub>4</sub>. *Appl. Phys. Lett.* **1994**, *65*, 676–678.
- (2) Cölle, M.; Brütting, W.; Schwoerer, M.; Yahiro, M.; Tsutsui, T. Electroluminescent Devices using a Layered Organic-Inorganic Perovskite Structure as Emitter. *Proc. SPIE* **2001**, *4105*, 328.
- (3) Tan, Z.-K.; Moghaddam, R. S.; Lai, M. L.; Docampo, P.; Higler, R.; Deschler, F.; Price, M.; Sadhanala, A.; Pazos, L. M.; Credgington, D.; Hanusch, F.; Bein, T.; Snaith, H. J.; Friend, R. H. Bright Light-Emitting Diodes Based on Organometal Halide Perovskite. *Nat. Nanotechnol.* **2014**, *9*, 687–692.
- (4) Liu, Y.; Cui, J.; Du, K.; Tian, H.; He, Z.; Zhou, Q.; Yang, Z.; Deng, Y.; Chen, D.; Zuo, X.; Ren, Y.; Wang, L.; Zhu, H.; Zhao, B.; Di, D.; Wang, J.; Friend, R. H.; Jin, Y. Efficient Blue Light-Emitting Diodes Based on Quantum-Confined Bromide Perovskite Nanostructures. *Nat. Photonics* **2019**, *13*, 760–764.
- (5) Liu, X.-K.; Xu, W.; Bai, S.; Jin, Y.; Wang, J.; Friend, R. H.; Gao, F. Metal Halide Perovskites for Light-Emitting Diodes. *Nat. Mater.* **2021**, *20*, 10–21.

- (6) Park, M.-H.; Kim, J. S.; Heo, J.-M.; Ahn, S.; Jeong, S.-H.; Lee, T.-W. Boosting Efficiency in Polycrystalline Metal Halide Perovskite Light-Emitting Diodes. *ACS Energy Letters* **2019**, *4*, 1134–1149.
- (7) Ji, K.; Anaya, M.; Abfalterer, A.; Stranks, S. D. Halide Perovskite Light-Emitting Diode Technologies. *Advanced Optical Materials* **2021**, *9*, 2002128.
- (8) Woo, S.-J.; Kim, J. S.; Lee, T.-W. Characterization of Stability and Challenges to Improve Lifetime in Perovskite LEDs. *Nat. Photonics* **2021**, *15*, 630–634.
- (9) Kim, Y.-H.; Kim, S.; Kakekhani, A.; Park, J.; Park, J.; Lee, Y.-H.; Xu, H.; Nagane, S.; Wexler, R. B.; Kim, D.-H.; Jo, S. H.; Martinez-Sarti, L.; Tan, P.; Sadhanala, A.; Park, G.-S.; Kim, Y.-W.; Hu, B.; Bolink, H. J.; Yoo, S.; Friend, R. H.; Rappe, A. M.; Lee, T.-W. Comprehensive Defect Suppression in Perovskite Nanocrystals for High-Efficiency Light-Emitting Diodes. *Nat. Photonics* **2021**, *15*, 148–155.
- (10) Ye, J.; Byranvand, M. M.; Martínez, C. O.; Hoye, R. L. Z.; Saliba, M.; Polavarapu, L. Defect Passivation in Lead-Halide Perovskite Nanocrystals and Thin Films: Toward Efficient LEDs and Solar Cells. *Angew. Chem.* **2021**, *133*, 21804–21828.
- (11) Protesescu, L.; Yakunin, S.; Bodnarchuk, M. I.; Krieg, F.; Caputo, R.; Hendon, C. H.; Yang, R. X.; Walsh, A.; Kovalenko, M. V. Nanocrystals of Cesium Lead Halide Perovskites (CsPbX<sub>3</sub>, X = Cl, Br, and I): Novel Optoelectronic Materials Showing Bright Emission with Wide Color Gamut. *Nano Lett.* **2015**, *15*, 3692–3696.
- (12) Gomez, L.; de Weerd, C.; Hueso, J. L.; Gregorkiewicz, T. Color-Stable Water-Dispersed Cesium Lead Halide Perovskite Nanocrystals. *Nanoscale* **2017**, *9*, 631–636.
- (13) Kumawat, N. K.; Swarnkar, A.; Nag, A.; Kabra, D. Ligand Engineering to Improve the Luminance Efficiency of CsPbBr<sub>3</sub> Nanocrystal Based Light-Emitting Diodes. *J. Phys. Chem. C* **2018**, *122*, 13767–13773.
- (14) Yan, W.; Shen, J.; Zhu, Y.; Gong, Y.; Zhu, J.; Wen, Z.; Li, C. CsPbBr<sub>3</sub> Quantum Dots Photodetectors Boosting Carrier Transport via Molecular Engineering Strategy. *Nano Research* **2021**, *14*, 4038–4045.
- (15) Li, G.; Huang, J.; Zhu, H.; Li, Y.; Tang, J.-X.; Jiang, Y. Surface Ligand Engineering for Near-Unity Quantum Yield Inorganic Halide Perovskite QDs and High-Performance QLEDs. *Chem. Mater.* **2018**, *30*, 6099–6107.
- (16) Li, F.; Liu, Y.; Wang, H.; Zhan, Q.; Liu, Q.; Xia, Z. Postsynthetic Surface Trap Removal of CsPbX<sub>3</sub> (X = Cl, Br, Or I) Quantum Dots via a ZnX<sub>2</sub>/Hexane Solution toward an Enhanced Luminescence Quantum Yield. *Chem. Mater.* **2018**, *30*, 8546–8554.
- (17) Mondal, N.; De, A.; Samanta, A. Achieving Near-Unity Photoluminescence Efficiency for Blue-Violet-Emitting Perovskite Nanocrystals. *ACS Energy Letters* **2019**, *4*, 32–39.
- (18) Das, S.; De, A.; Samanta, A. Ambient Condition Mg<sup>2+</sup> Doping Producing Highly Luminescent Green- and Violet-Emitting Perovskite Nanocrystals with Reduced Toxicity and Enhanced Stability. *J. Phys. Chem. Lett.* **2020**, *11*, 1178–1188.
- (19) van der Stam, W.; Geuchies, J. J.; Altantzis, T.; van den Bos, K. H. W.; Meeldijk, J. D.; Van Aert, S.; Bals, S.; Vanmaekelbergh, D.; de Mello Donega, C. Highly Emissive Divalent-Ion-Doped Colloidal CsPb<sub>1-x</sub>M<sub>x</sub>Br<sub>3</sub> Perovskite Nanocrystals through Cation Exchange. *J. Am. Chem. Soc.* **2017**, *139*, 4087–4097.
- (20) Wu, T.; Li, J.; Zou, Y.; Xu, H.; Wen, K.; Wan, S.; Bai, S.; Song, T.; McLeod, J. A.; Duhm, S.; Gao, F.; Sun, B. High-Performance Perovskite Light-Emitting Diode with Enhanced Operational Stability Using Lithium Halide Passivation. *Angew. Chem., Int. Ed.* **2020**, *59*, 4099–4105.
- (21) Wu, H.; Qiu, J.; Wang, J.; Wen, Y.; Wang, Q.; Long, Z.; Zhou, D.; Yang, Y.; Wang, D. The Dual-Defect Passivation Role of Lithium Bromide Doping in Reducing the Nonradiative Loss in CsPbX<sub>3</sub> (X = Br and I) Quantum Dots. *Inorganic Chemistry Frontiers* **2021**, *8*, 658–668.
- (22) Chen, C.; Yang, G.; Ma, J.; Zheng, X.; Chen, Z.; Zhang, Q.; Fang, G. Surface Treatment via Li-bis-(trifluoromethanesulfonyl)-imide to Eliminate the Hysteresis and Enhance the Efficiency of Inverted Perovskite Solar Cells. *J. Mater. Chem. C* **2017**, *5*, 10280–10287.
- (23) Luo, H.; Wu, J.; Liu, Q.; Zhang, M.; Yuan, P.; Huang, M. An Additive of Sulfonic Lithium Salt for High-Performance Perovskite Solar Cells. *ChemistrySelect* **2018**, *3*, 12320–12324.
- (24) Pham, N. D.; Shang, J.; Yang, Y.; Hoang, M. T.; Tjong, V. T.; Wang, X.; Fan, L.; Chen, P.; Kou, L.; Wang, L.; Wang, H. Alkaline-Earth Bis(trifluoromethanesulfonimide) Additives for Efficient and Stable Perovskite Solar Cells. *Nano Energy* **2020**, *69*, 104412.
- (25) Liu, M.; Ma, L.; Xie, K.; Zeng, P.; Wei, S.; Zhang, F.; Li, C.; Wang, F. Efficiently Improved Photoluminescence in Cesium Lead Halide Perovskite Nanocrystals by Using Bis(trifluoromethane)-sulfonimide. *J. Phys. Chem. Lett.* **2022**, *13*, 1519–1525.
- (26) Nguyen, T.P.; Le Rendu, P.; Long, P.D.; De Vos, S.A. Chemical and Thermal Treatment of PEDOT:PSS Thin Films for Use in Organic Light Emitting Diodes. *Surf. Coat. Technol.* **2004**, *180–181*, 646–649.
- (27) Peng, X.-F.; Wu, X.-Y.; Ji, X.-X.; Ren, J.; Wang, Q.; Li, G.-Q.; Yang, X.-H. Modified Conducting Polymer Hole Injection Layer for High-Efficiency Perovskite Light-Emitting Devices: Enhanced Hole Injection and Reduced Luminescence Quenching. *J. Phys. Chem. Lett.* **2017**, *8*, 4691–4697.
- (28) Olthof, S. Reactive Interfaces: Perovskite Degradation at Metal-Oxide Interfaces Probed by Photoelectron Spectroscopy. *Organic and Hybrid Light Emitting Materials and Devices XXV*; SPIE: Bellingham, WA, 2021.
- (29) Kim, K.; Jeong, J.; Kim, M.; Kang, D.; Cho, S. W.; Lee, H.; Yi, Y. Direct p-Doping of Li-TFSI for Efficient Hole Injection: Role of Polaronic Level in Molecular Doping. *Appl. Surf. Sci.* **2019**, *480*, 565–571.
- (30) Zhao, B.; Lian, Y.; Cui, L.; Divitini, G.; Kusch, G.; Ruggeri, E.; Auras, F.; Li, W.; Yang, D.; Zhu, B.; Oliver, R. A.; MacManus-Driscoll, J. L.; Stranks, S. D.; Di, D.; Friend, R. H. Efficient Light-Emitting Diodes from Mixed-Dimensional Perovskites on a Fluoride Interface. *Nature Electronics* **2020**, *3*, 704–710.
- (31) Sun, Y.; Zhang, H.; Zhu, K.; Ye, W.; She, L.; Gao, X.; Ji, W.; Zeng, Q. Research on the Influence of Polar Solvents on CsPbBr<sub>3</sub> Perovskite QDs. *RSC Adv.* **2021**, *11*, 27333–27337.
- (32) Wahl, J.; Engelmayr, M.; Mandal, M.; Naujoks, T.; Haizmann, P.; Maier, A.; Peisert, H.; Andrienko, D.; Brütting, W.; Scheele, M. Porphyrin Functionalization of CsPbBr<sub>2</sub>/SiO<sub>2</sub> Core-Shell Nanocrystals Enhances the Stability and Efficiency in Electroluminescent Devices. *Advanced Optical Materials* **2022**, *10*, 2101945.
- (33) Hills-Kimball, K.; Yang, H.; Cai, T.; Wang, J.; Chen, O. Recent Advances in Ligand Design and Engineering in Lead Halide Perovskite Nanocrystals. *Advanced Science* **2021**, *8*, 2100214.
- (34) Dutta, A.; Behera, R. K.; Pal, P.; Baitalik, S.; Pradhan, N. Near-Unity Photoluminescence Quantum Efficiency for All CsPbX<sub>3</sub> (X = Cl, Br, and I) Perovskite Nanocrystals: A Generic Synthesis Approach. *Angew. Chem.* **2019**, *131*, 5608–5612.
- (35) Akkerman, Q. A.; D'Innocenzo, V.; Accornero, S.; Scarpellini, A.; Petrozza, A.; Prato, M.; Manna, L. Tuning the Optical Properties of Cesium Lead Halide Perovskite Nanocrystals by Anion Exchange Reactions. *J. Am. Chem. Soc.* **2015**, *137*, 10276–10281.
- (36) Di Stasio, F.; Christodoulou, S.; Huo, N.; Konstantatos, G. Near-Unity Photoluminescence Quantum Yield in CsPbBr<sub>3</sub> Nanocrystal Solid-State Films via Postsynthesis Treatment with Lead Bromide. *Chem. Mater.* **2017**, *29*, 7663–7667.
- (37) Woo, J. Y.; Kim, Y.; Bae, J.; Kim, T. G.; Kim, J. W.; Lee, D. C.; Jeong, S. Highly Stable Cesium Lead Halide Perovskite Nanocrystals through in Situ Lead Halide Inorganic Passivation. *Chem. Mater.* **2017**, *29*, 7088–7092.
- (38) Schmidt, T. D.; Lampe, T.; Sylvinson, M. R., D.; Djurovich, P. I.; Thompson, M. E.; Brütting, W. Emitter Orientation as a Key Parameter in Organic Light-Emitting Diodes. *Physical Review Applied* **2017**, *8*, 037001.
- (39) Jurow, M. J.; Morgenstern, T.; Eisler, C.; Kang, J.; Penzo, E.; Do, M.; Engelmayr, M.; Osowiecki, W. T.; Bekenstein, Y.; Tassone, C.; Wang, L.-W.; Alivisatos, A. P.; Brütting, W.; Liu, Y. Manipulating

the Transition Dipole Moment of CsPbBr<sub>3</sub> Perovskite Nanocrystals for Superior Optical Properties. *Nano Lett.* **2019**, *19*, 2489–2496.

(40) Jagielski, J.; Solari, S. F.; Jordan, L.; Scullion, D.; Blülle, B.; Li, Y.-T.; Krumeich, F.; Chiu, Y.-C.; Ruhstaller, B.; Santos, E. J. G.; Shih, C.-J. Scalable Photonic Sources using Two-Dimensional Lead Halide Perovskite Superlattices. *Nat. Commun.* **2020**, *11*, 387.

(41) Morgenstern, T.; Lampe, C.; Naujoks, T.; Jurow, M.; Liu, Y.; Urban, A. S.; Brütting, W. Elucidating the Performance Limits of Perovskite Nanocrystal Light Emitting Diodes. *J. Lumin.* **2020**, *220*, 116939.

(42) Jurow, M. J.; Lampe, T.; Penzo, E.; Kang, J.; Koc, M. A.; Zechel, T.; Nett, Z.; Brady, M.; Wang, L.-W.; Alivisatos, A. P.; Cabrini, S.; Brütting, W.; Liu, Y. Tunable Anisotropic Photon Emission from Self-Organized CsPbBr<sub>3</sub> Perovskite Nanocrystals. *Nano Lett.* **2017**, *17*, 4534–4540.

(43) Tavares, T. B.; de Sousa, F. F.; Sales, M. J. A.; Paterno, L. G.; Paschoal, W.; Moreira, S. G. C. Optical and Morphological Features of Poly(vinyl Carbazole)/Ferrite Composites for Potential Opto-Electronic Applications. *Appl. Phys. A: Mater. Sci. Process.* **2021**, *127*, 855.

(44) Olthof, S.; Meerholz, K. Substrate-Dependent Electronic Structure and Film Formation of MAPbI<sub>3</sub> Perovskites. *Sci. Rep.* **2017**, *7*, 40267.

(45) Zu, F.; Wolff, C. M.; Ralaiarisoa, M.; Amsalem, P.; Neher, D.; Koch, N. Unraveling the Electronic Properties of Lead Halide Perovskites with Surface Photovoltage in Photoemission Studies. *ACS Appl. Mater. Interfaces* **2019**, *11*, 21578–21583.

(46) Endres, J.; Egger, D. A.; Kulbak, M.; Kerner, R. A.; Zhao, L.; Silver, S. H.; Hodes, G.; Rand, B. P.; Cahen, D.; Kronik, L.; Kahn, A. Valence and Conduction Band Densities of States of Metal Halide Perovskites: A Combined Experimental–Theoretical Study. *J. Phys. Chem. Lett.* **2016**, *7*, 2722–2729.

(47) Zu, F.; Amsalem, P.; Egger, D. A.; Wang, R.; Wolff, C. M.; Fang, H.; Loi, M. A.; Neher, D.; Kronik, L.; Duhm, S.; Koch, N. Constructing the Electronic Structure of CH<sub>3</sub>NH<sub>3</sub>PbI<sub>3</sub> and CH<sub>3</sub>NH<sub>3</sub>PbBr<sub>3</sub> Perovskite Thin Films from Single-Crystal Band Structure Measurements. *J. Phys. Chem. Lett.* **2019**, *10*, 601–609.

(48) Cao, J.; Tao, S. X.; Bobbert, P. A.; Wong, C.-P.; Zhao, N. Interstitial Occupancy by Extrinsic Alkali Cations in Perovskites and Its Impact on Ion Migration. *Adv. Mater.* **2018**, *30*, 1707350.

(49) An, R.; Zhang, F.; Zou, X.; Tang, Y.; Liang, M.; Oshchapovskyy, I.; Liu, Y.; Honarfar, A.; Zhong, Y.; Li, C.; Geng, H.; Chen, J.; Canton, S. E.; Pullerits, T.; Zheng, K. Photostability and Photodegradation Processes in Colloidal CsPbI<sub>3</sub> Perovskite Quantum Dots. *ACS Appl. Mater. Interfaces* **2018**, *10*, 39222–39227.

(50) Fang, Z.; He, H.; Gan, L.; Li, J.; Ye, Z. Understanding the Role of Lithium Doping in Reducing Nonradiative Loss in Lead Halide Perovskites. *Advanced Science* **2018**, *5*, 1800736.

(51) Pointon, A. I.; Grant, N. E.; Bonilla, R. S.; Wheeler-Jones, E. C.; Walker, M.; Wilshaw, P. R.; Dancer, C. E. J.; Murphy, J. D. Exceptional Surface Passivation Arising from Bis-(trifluoromethanesulfonyl)-Based Solutions. *ACS Applied Electronic Materials* **2019**, *1*, 1322–1329.

(52) Chu, H.; Noh, H.; Kim, Y.-J.; Yuk, S.; Lee, J.-H.; Lee, J.; Kwack, H.; Kim, Y.; Yang, D.-K.; Kim, H.-T. Achieving Three-Dimensional Lithium Sulfide Growth in Lithium-Sulfur Batteries using High-Donor-Number Anions. *Nat. Commun.* **2019**, *10*, 188.

(53) Lamberti, F.; Gatti, T.; Cescon, E.; Sorrentino, R.; Rizzo, A.; Menna, E.; Meneghesso, G.; Meneghetti, M.; Petrozza, A.; Franco, L. Evidence of Spiro-OMeTAD De-Doping by Tert-Butylpyridine Additive in Hole-Transporting Layers for Perovskite Solar Cells. *Chem.* **2019**, *5*, 1806–1817.

(54) Kong, J.; Shin, Y.; Röhr, J. A.; Wang, H.; Meng, J.; Wu, Y.; Katzenberg, A.; Kim, G.; Kim, D. Y.; Li, T.-D.; Chau, E.; Antonio, F.; Siboonruang, T.; Kwon, S.; Lee, K.; Kim, J. R.; Modestino, M. A.; Wang, H.; Taylor, A. D. CO<sub>2</sub> Doping of Organic Interlayers for Perovskite Solar Cells. *Nature* **2021**, *594*, 51–56.

(55) Ravi, V. K.; Markad, G. B.; Nag, A. Band Edge Energies and Excitonic Transition Probabilities of Colloidal CsPbX<sub>3</sub> (X = Cl, Br, I) Perovskite Nanocrystals. *ACS Energy Letters* **2016**, *1*, 665–671.

(56) Rainò, G.; Landuyt, A.; Krieg, F.; Bernasconi, C.; Ochsenbein, S. T.; Dirin, D. N.; Bodnarchuk, M. I.; Kovalenko, M. V. Underestimated Effect of a Polymer Matrix on the Light Emission of Single CsPbBr<sub>3</sub> Nanocrystals. *Nano Lett.* **2019**, *19*, 3648–3653.

(57) Pierini, S.; D'Amato, M.; Goyal, M.; Glorieux, Q.; Giacobino, E.; Lhuillier, E.; Couteau, C.; Bramati, A. Highly Photostable Perovskite Nanocubes: Toward Integrated Single Photon Sources Based on Tapered Nanofibers. *ACS Photonics* **2020**, *7*, 2265–2272.

(58) Samu, G. F.; Scheidt, R. A.; Kamat, P. V.; Janáky, C. Electrochemistry and Spectroelectrochemistry of Lead Halide Perovskite Films: Materials Science Aspects and Boundary Conditions. *Chem. Mater.* **2018**, *30*, 561–569.

(59) Mulder, J. T.; du Fosse, I.; Alimoradi Jazi, M.; Manna, L.; Houtepen, A. J. Electrochemical p-Doping of CsPbBr<sub>3</sub> Perovskite Nanocrystals. *ACS Energy Letters* **2021**, *6*, 2519–2525.

(60) Hasnidawani, J.; Azlina, H.; Norita, H.; Bonnia, N.; Ratim, S.; Ali, E. Synthesis of ZnO Nanostructures Using Sol-Gel Method. *Procedia Chemistry* **2016**, *19*, 211–216.

(61) Maes, J.; Balcaen, L.; Drijvers, E.; Zhao, Q.; De Roo, J.; Vantomme, A.; Vanhaecke, F.; Geiregat, P.; Hens, Z. Light Absorption Coefficient of CsPbBr<sub>3</sub> Perovskite Nanocrystals. *J. Phys. Chem. Lett.* **2018**, *9*, 3093–3097.

(62) Leyre, S.; Coutino-Gonzalez, E.; Joos, J. J.; Ryckaert, J.; Meuret, Y.; Poelman, D.; Smet, P. F.; Durinck, G.; Hofkens, J.; Deconinck, G.; Hanselaer, P. Absolute Determination of Photoluminescence Quantum Efficiency using an Integrating Sphere Setup. *Rev. Sci. Instrum.* **2014**, *85*, 123115.